

Ab initio calculations of photocurrent in solids based on Wannier function

Junqing Xu^{1,*} and Haixiao Xiao^{1,†}

¹*Department of Physics, Hefei University of Technology, Hefei, Anhui, China*

(Dated: March 5, 2024)

We present a general *ab initio* method based on Wannier function for simulating the photocurrent in solids. The method is widely applicable to charge/spin DC and AC photocurrent at any perturbation levels in both semiconductors and metals for both linearly and circularly polarized light. This is because the method is theoretically complete (within relaxation time approximation), that is to say, it includes all intra-band, inter-band and their cross terms. Specifically for the second-order DC photocurrent, it includes all of the following contributions - shift current, (magnetic) injection current, Berry curvature dipole, gyration current and Fermi surface ones, instead of only a part of them as in most previous *ab initio* methods. It is also free from the degeneracy issue, i.e., applicable to arbitrary band structures with arbitrary numbers of degenerate bands. We apply the method to various semiconductors and metals, including GaAs, graphene-hBN heterostructure, monolayer WS₂, a 2D ferroelectric material - monolayer GeS, bilayer anti-ferromagnetic MnBi₂Te₄ and topological Weyl semimetal RhSi to simulate their charge and/or spin, DC and/or AC photocurrent. Our theoretical results are in good agreement with previous theoretical works. Our method provides a universal computational tool for reliable and accurate predictions of abundant weak-field photocurrent phenomena in disparate materials.

I. INTRODUCTION

The electric current generation under uniform light illumination, called photocurrent, have been extensively studied in optoelectronic physics.[1–11] Recently, the photocurrent phenomena in solids, such as bulk photovoltaic effect (BPVE, also called photogalvanic effect - PGE), second- and third-harmonic generation (SHG and THG) and sum-/difference-frequency generation, have drawn much attention in the research fields of condensed matter physics, opto-electronics, opto-spintronics, material science, etc. For example, quantized circular photogalvanic effect (CPGE), whereby circular polarized light generates a helicity-dependent photocurrent, in Weyl semimetals were predicted[4] and observed[5]. Spin-valley-coupled CPGE and its electric control was realized in WSe₂. [6] Robust pure spin photocurrent was predicted in several materials.[7, 12] Electrically and broadband tunable third-harmonic generation was realized in graphene.[13]

In this work we focus on the photocurrent under weak fields, since such conditions are usually satisfied in the studies of BPVE and low-order harmonic generation (LHG) and are preferred for the related low-power optical device applications. Moreover, the weak-field photocurrent measurements are invaluable in detecting materials' properties such as topological and spin ones. This is because the weak-field photocurrent is simply the product of electric fields and optical susceptibilities, and the latter are a class of materials' properties determined by band structure, Berry connections, spin-orbit coupling, the scattering strength, etc.

Predictive *ab initio* theories based on density functional theory (DFT) appeared since the late 1990s for SHG[9, 14] and since the early 2010s for BPVE[2, 12, 15]. These theories are invaluable for the understandings of experimental findings and the predictions of new materials with excellent properties. The main challenge of *ab initio* calculations is that very dense k-point samplings are often required to converge the results, e.g., 10⁶ k-points may be necessary for topological semimetals, which makes them computationally expensive. The k-point convergence issue becomes more serious if *ab initio* sophisticated forms of the scattering/relaxation processes beyond the simple relaxation time approximation (RTA) are employed.

To resolve this issue, *ab initio* methods using maximally localized Wannier function have been employed for efficient calculation of the shift current, injection current and Berry curvature dipole contributions to the photocurrent.[16–20] However, the current Wannier-function-based methods have two main problems: (i) Some important contributions to BPVE, e.g., the intrinsic Fermi surface effect and the gyration current proposed by Watanabe and Yanase[21], are not considered and the implementations for LHG are even less complete. Therefore, large errors may present in the studies of metallic systems and/or under circularly polarized light. (ii) The Wannier interpolation of Berry connection (needed in their methods) uses the nondegenerate perturbation theory, so that the degenerate bands are not treated properly.

The above problems can be removed by employing a technique originally developed for theoretical simulations of high harmonic generation under strong fields in Ref. 9, where the laser term of the electron dynamics is first expressed in the smooth “Wannier” representation and then transformed to the eigenstate representation. In “Wannier” representation, the basis are smooth Bloch-

* jqxu@hfut.edu.cn

† xiaohx@hfut.edu.cn

like functions of \mathbf{k} , so that the laser term (in the length gauge) is well defined and can be easily computed by finite difference. Therefore, the degeneracy issue is bypassed. Moreover, with the accurate expression of the laser term, all contributions to the photocurrent within RTA, including the shift current, (magnetic) injection current, Berry curvature dipole, gyration current and Fermi surface contributions, can be considered.

Therefore, it is promising to apply the technique of Ref. 9 to other photocurrent properties besides HHG. Here, we thus have developed an *ab initio* method based on Wannier function of the photocurrent including BPVE and LHG within RTA. The method is applicable to both semiconductors and metals for both linearly and circularly polarized light, corresponding to linearly PGE (LPGE) and CPGE respectively.

This article is organized as follows. In Sec. II, we derive the formulae of optical susceptibilities via perturbative treatment of the density-matrix (DM) master equation in the length gauge within RTA. We then relates the second-order susceptibilities to LPGE and CPGE. In Sec. III, we given the computational setups of our DFT and photocurrent calculations. In Sec. IV, we apply our method to various semiconductors and metals, including GaAs, graphene-hBN heterostructure, monolayer WS₂, a 2D ferroelectric material - monolayer GeS, bilayer anti-ferromagnetic MnBi₂Te₄ and topological Weyl semimetal RhSi to simulate their charge and/or spin BPVE and LHG. In Sec. V, a summary and outlooks are given.

II. METHODS

Theoretically, the photocurrent formulae can be expressed in both the length and velocity gauges for the laser.[22] In most theoretical works, the length gauge was employed. This is because that although the velocity gauge has simpler formulae, it suffers from several issues: (i) Large number of bands are required to converge the results if additional calculations are not employed;[12, 23] (ii) The dephasing and the general scattering term beyond relaxation time approximation (RTA) are hard to be included;[24] (iii) The numerical results may diverge at low- ω (photon frequency) limit.[22]

In length gauge, the current density $\mathbf{J}^c(t)$ and spin-current density $\mathbf{J}^{s\gamma}(t)$ are

$$\mathbf{J}^{c/s\gamma}(t) = V_{\text{cell}}^{-1} \text{Tr} \left[\mathbf{j}^{c/s\gamma} \rho(t) \right], \quad (1)$$

$$\mathbf{j}^c = -e\mathbf{v}, \quad (2)$$

$$\mathbf{v} = \frac{-i}{\hbar} [\mathbf{r}, H^0], \quad (3)$$

$$\mathbf{j}^{s\gamma} = 0.5 \times (s_\gamma \mathbf{v} + \mathbf{v} s_\gamma), \quad (4)$$

where ρ is the DM of Bloch electrons. V_{cell} is the unit-cell volume/area of the crystal for 3D/2D systems. \mathbf{j}^c is the charge current operator. \mathbf{v} is the velocity operator. \mathbf{r} is the position operator, H is Hamiltonian operator and

H^0 is unperturbed Hamiltonian operator. In the eigenbasis, $H_{kab}^0 = \epsilon_{ka} \delta_{ab}$ with ϵ the eigenvalue, k the k-point index and a (b) the band index. s_γ is the spin operator along γ direction. $\mathbf{j}^{s\gamma}$ is the conventional spin-current operator[25].

A. DM master equation in the length gauge

We solve the quantum master equation of the single-particle $\rho(t)$ in the Schrödinger picture as[22, 26, 27]

$$\frac{d\rho(t)}{dt} = -\frac{i}{\hbar} [H^0, \rho(t)] + D^E[\rho] + C[\rho], \quad (5)$$

$$D^E[\rho] = \frac{e}{\hbar} \mathbf{E}(t) \cdot \frac{D\rho}{D\mathbf{k}}, \quad (6)$$

where $D^E[\rho]$ and $C[\rho]$ is the laser and collision terms of the DM dynamics respectively. $\mathbf{E}(t)$ is the time-dependent electric field of a laser. $\frac{D\rho}{D\mathbf{k}}$ is the covariant derivative of ρ .

For a laser with photon frequency ω ,

$$\mathbf{E}(t) = \mathbf{E}(\omega) e^{i\omega t} + \mathbf{E}(-\omega) e^{-i\omega t} \quad (7)$$

with $\mathbf{E}(-\omega) \equiv \mathbf{E}^*(\omega)$ being the constant amplitude.

The covariant derivative of an arbitrary operator A - $\frac{DA}{D\mathbf{k}}$ is defined as[22]

$$\frac{DA}{D\mathbf{k}} = \frac{dA}{d\mathbf{k}} - i[\xi, A], \quad (8)$$

$$\xi_{kab} = i \left\langle u_{ka} \left| \frac{du_{kb}}{d\mathbf{k}} \right. \right\rangle, \quad (9)$$

where $\frac{d}{d\mathbf{k}}$ is the gradient, ξ is the Berry connection and u is the basis function or the periodic part of Bloch wavefunction. Note that Eq. 8 above is the same as Eq. 34 of Ref. 22, but different notations are used. The operator $\frac{D}{D\mathbf{k}}$ is directly related to the position operator \mathbf{r} as follow:

$$\frac{DA}{D\mathbf{k}} = -i[\mathbf{r}, A]. \quad (10)$$

Therefore, the electric-field term of the master equation $D^E[\rho]$ can be expressed as

$$D^E[\rho] = -\frac{i}{\hbar} [H^E, \rho], \quad (11)$$

$$H^E = e\mathbf{E}(t) \cdot \mathbf{r}. \quad (12)$$

The computation of $\frac{D\rho}{D\mathbf{k}}$ via Eq. 8 is non-trivial due to the following issues: First, the basis functions u_k are usually obtained by diagonalizing H_k^0 at different \mathbf{k} independently, so that u_k contain arbitrary phase factors and are arbitrary in degenerate subspaces. Therefore, u_k are in general not smooth over \mathbf{k} , which makes $\frac{d\rho}{d\mathbf{k}}$ not well-defined (except when $\rho = f^{\text{eq}}$). Second, the computation of ξ may suffer from the degeneracy issue,

as discussed later in Sec. IID 1. The above issues are bypassed through the use of a Wannier-function-based technique given below in Sec. IID 2.

The collision term $C[\rho]$ of Eq. 5 describes the decay of ρ to its equilibrium due to various processes such as the electron-phonon scattering, the electron-hole recombination, etc. In this work, we approximate $C[\rho]$ within RTA as

$$C[\rho] = -\Gamma \odot \{\rho - f^{\text{eq}}\}, \quad (13)$$

where f^{eq} is the equilibrium part of ρ and a diagonal matrix whose elements are Fermi-Dirac functions. Γ is the relaxation rate matrix and Γ_{kaa} is the relaxation rate of the electronic state $(k, a) - \Gamma_{ka}$. Hadamard product $A \odot B$ means the elementwise multiplication of matrices A and B .

Suppose

$$\rho = f^{\text{eq}} + \rho^E. \quad (14)$$

Considering that $\frac{df^{\text{eq}}}{dt} = 0$ and $[\epsilon, f^{\text{eq}}] = 0$, within RTA, Eq. 5 becomes

$$i\hbar \frac{d\rho^E}{dt} + (i\hbar\Gamma - \Delta) \odot \rho^E = ie\mathbf{E}(t) \cdot \frac{D\rho}{D\mathbf{k}}, \quad (15)$$

$$\Delta_{kab} = \epsilon_{ka} - \epsilon_{kb}. \quad (16)$$

B. Perturbative solution of ρ^E and optical susceptibility for charge and spin current

At weak fields, ρ can be expanded as $\rho = \sum_n \rho^{(n)}$ with $\rho^{(n)} = O(|\mathbf{E}(\omega)|^n)$ and $\rho^{(0)} \equiv f^{\text{eq}}$. Therefore, the n th-order master equation is

$$i\hbar \frac{d\rho^{E,(n)}}{dt} + (i\hbar\Gamma - \Delta) \odot \rho^{E,(n)} = ie\mathbf{E}(t) \cdot \frac{D\rho^{(n-1)}}{D\mathbf{k}}, \quad (17)$$

$$\rho^{E,(n)} = (1 - \delta_{n0}) \rho^{(n)}. \quad (18)$$

The above equation is a first-order (for the time derivative) ordinary differential equation. If the minimum element of $\Gamma - \Gamma_{\text{min}}$ is positive. At $t \gg \Gamma_{\text{min}}^{-1}$, Eq. 17 has a stationary solution

$$\rho^{E,(n)}(t) = \sum_m \rho^{E,(n)}(m\omega) e^{im\omega t}, \quad (19)$$

where $\rho^{E,(n)}(m\omega)$ is time-independent. Therefore, at $t \gg \Gamma_{\text{min}}^{-1}$, from Eq. 17,

$$\begin{aligned} & (-m\hbar\omega - \Delta + i\hbar\Gamma) \odot \rho^{E,(n)}(m\omega) \\ & = ie \sum_{\pm} \mathbf{E}(\pm\omega) \cdot \frac{D\rho^{(n-1)}((m \mp 1)\omega)}{D\mathbf{k}}. \end{aligned} \quad (20)$$

Define

$$d_{kab}^{\Gamma}(\omega) = \frac{1}{-\hbar\omega - \Delta_{kab} + i\hbar\Gamma_{kab}}, \quad (21)$$

we have,

$$\begin{aligned} \rho^{E,(n)}(m\omega) & = ie \sum_{\pm} \mathbf{E}(\pm\omega) \cdot \frac{D\rho^{(n-1)}((m \mp 1)\omega)}{D\mathbf{k}} \\ & \odot d^{\Gamma}(m\omega), \end{aligned} \quad (22)$$

From the above equation, we can define a n th-order DM from the following iterative formulae,

$$\rho_{\alpha_1 \dots \alpha_n}^{E,(n)}(\omega_1, \dots, \omega_n) = \left\{ \begin{array}{l} ie E_{\alpha_1}(\omega_1) \frac{D\rho_{\alpha_2 \dots \alpha_n}^{(n-1)}(\omega_2, \dots, \omega_n)}{Dk_{\alpha_1}} \\ \odot d^{\Gamma}\left(\sum_{j=1}^n \omega_j\right) \end{array} \right\}, \quad (23)$$

$$\rho_{\alpha_n}^{E,(1)}(\omega_n) = ie E_{\alpha_n}(\omega_n) \frac{D\rho^{(0)}}{Dk_{\alpha_n}} \odot d^{\Gamma}(\omega_n), \quad (24)$$

$$\omega_j = \pm \omega. \quad (25)$$

We further define the normalized n th-order DM as

$$\tilde{\rho}_{\alpha_1 \dots \alpha_n}^{E,(n)}(\omega_1, \dots, \omega_n) = \frac{\rho_{\alpha_1 \dots \alpha_n}^{E,(n)}(\omega_1, \dots, \omega_n)}{\prod_i E_{\alpha_i}(\omega_i)}. \quad (26)$$

Therefore, the n th-order current and spin-current densities can be expressed as

$$\mathbf{J}^{c/s_{\gamma},(n)}(t) = \sum_m \mathbf{J}^{c/s_{\gamma},(n)}(m\omega) e^{im\omega t}, \quad (27)$$

$$\mathbf{J}^{c/s_{\gamma},(n)}\left(\sum_{j=1}^n \omega_j\right) = V_{\text{cell}}^{-1} \prod_i^n E_{\alpha_i}(\omega_i) \quad (28)$$

$$\times \text{Tr} \left[\mathbf{j}^{c/s_{\gamma}} \tilde{\rho}_{\alpha_1 \dots \alpha_n}^{E,(n)}(\omega_1, \dots, \omega_n) \right]. \quad (29)$$

Since n th-order optical susceptibilities for charge and spin current are defined as

$$\mathbf{J}_{\beta}^{c/s_{\gamma},(n)}\left(\sum_{j=1}^n \omega_j\right) = \sum_{\alpha_1 \dots \alpha_n} \prod_i^n E_{\alpha_i}(\omega_i) \sigma_{\alpha_1 \dots \alpha_n}^{c/s_{\gamma},\beta}(\omega_1, \dots, \omega_n), \quad (30)$$

we have

$$\sigma_{\alpha_1 \dots \alpha_n}^{c/s_{\gamma},\beta}(\omega_1, \dots, \omega_n) = V_{\text{cell}}^{-1} \text{Tr} \left[\mathbf{j}_{\beta}^{c/s_{\gamma}} \tilde{\rho}_{\alpha_1 \dots \alpha_n}^{E,(n)}(\omega_1, \dots, \omega_n) \right]. \quad (31)$$

From the above equations, we can obtain arbitrary-order perturbative optical susceptibilities and photocurrent. Considering that BPVE, SHG and THG, three of the most important photocurrent phenomena, are determined by second- and third-order optical susceptibilities, we present the detailed formulae of optical susceptibilities in first three orders in the following.

1. First-order

From Eq. 24, 26 and 31, we have

$$\tilde{\rho}_{\alpha}^{E,(1)}(\omega) = ie \frac{Df^{\text{eq}}}{Dk_{\alpha}} \odot d^{\Gamma}(\omega), \quad (32)$$

$$\sigma_{\alpha}^{c/s_{\gamma},\beta}(\omega) = ie V_{\text{cell}}^{-1} \text{Tr} \left[j_{\beta}^{c/s_{\gamma}} \frac{Df^{\text{eq}}}{Dk_{\alpha}} \odot d^{\Gamma}(\omega) \right]. \quad (33)$$

$\sigma_{\alpha}^{c/s_{\gamma},\beta}(\omega)$ determines the optical conductivity.

2. Second-order

From Eq. 23, 24, 26 and 31, we have the DC component

$$\tilde{\rho}_{\alpha_1\alpha_2}^{E,(2)}(-\omega, \omega) = ie \frac{\tilde{\rho}_{\alpha_2}^{E,(1)}(\omega)}{Dk_{\alpha_1}} \odot d^{\Gamma}(0), \quad (34)$$

$$\sigma_{\alpha_1\alpha_2}^{c/s_{\gamma},\beta}(-\omega, \omega) = V_{\text{cell}}^{-1} \text{Tr} \left[j_{\beta}^{c/s_{\gamma}} \tilde{\rho}_{\alpha_1\alpha_2}^{E,(2)}(-\omega, \omega) \right]. \quad (35)$$

and the 2ω AC component

$$\tilde{\rho}_{\alpha_1\alpha_2}^{E,(2)}(\omega, \omega) = ie \frac{\tilde{\rho}_{\alpha_2}^{E,(1)}(\omega)}{Dk_{\alpha_1}} \odot d^{\Gamma}(2\omega), \quad (36)$$

$$\sigma_{\alpha_1\alpha_2}^{c/s_{\gamma},\beta}(\omega, \omega) = V_{\text{cell}}^{-1} \text{Tr} \left[j_{\beta}^{c/s_{\gamma}} \tilde{\rho}_{\alpha_1\alpha_2}^{E,(2)}(\omega, \omega) \right]. \quad (37)$$

$\sigma_{\alpha_1\alpha_2}^{c/s_{\gamma},\beta}(-\omega, \omega)$ and $\sigma_{\alpha_1\alpha_2}^{c/s_{\gamma},\beta}(\omega, \omega)$ determine BPVE and SHG respectively.

3. Third-order

From Eq. 23, 24, 26 and 31, we have the 3ω AC component

$$\tilde{\rho}_{\alpha_1\alpha_2\alpha_3}^{E,(3)}(\omega, \omega, \omega) = ie \frac{\tilde{\rho}_{\alpha_2\alpha_3}^{E,(2)}(\omega, \omega)}{Dk_{\alpha_1}} \odot d^{\Gamma}(3\omega), \quad (38)$$

$$\sigma_{\alpha_1\alpha_2\alpha_3}^{c/s_{\gamma},\beta}(\omega, \omega, \omega) = V_{\text{cell}}^{-1} \text{Tr} \left[j_{\beta}^{c/s_{\gamma}} \tilde{\rho}_{\alpha_1\alpha_2\alpha_3}^{E,(3)}(\omega, \omega, \omega) \right]. \quad (39)$$

$\sigma_{\alpha_1\alpha_2\alpha_3}^{c/s_{\gamma},\beta}(\omega, \omega, \omega)$ determines THG.

Under weak fields, the photocurrent mechanisms can be separated into two classes[2] - (i) One is described using the single-particle electronic quantities and with the scattering in Born approximation. The scattering is usually further simplified within RTA. (ii) Another is due to the asymmetric scattering beyond Born approximation and is called ballistic current. Since the former class seems more important in more cases and *ab initio* simulations of ballistic current are numerically difficult[28], most *ab initio* works only consider the former class of mechanisms[21].

The former class can be further separated into various types of contributions depending on if intra-

or inter-band parts of $\frac{D\rho}{D\mathbf{k}}$ and/or $j_{\beta}^{c/s_{\gamma}}$ matrices are considered.[21] See intra- and inter-band parts of $\frac{D\rho}{D\mathbf{k}}$ in Appendix A. For BPVE, the separation of different contributions is systematically discussed in Ref. 21 and the following contributions are identified: the shift current, (magnetic) injection current, Berry curvature dipole, gyration current and Fermi surface contributions. Since our method includes both intra- and inter-band parts of $\frac{D\rho}{D\mathbf{k}}$ and $j_{\beta}^{c/s_{\gamma}}$ matrices, all types of contributions belonging to the former class are considered.

C. LPGE and CPGE

Since the electric field amplitudes $\mathbf{E}(\pm\omega)$ of the linearly polarized light satisfy $E_{\alpha_1}(-\omega)E_{\alpha_2}(\omega) \equiv E_{\alpha_1}^*(\omega)E_{\alpha_2}(\omega)$ is real for any α_1 and α_2 and $\mathbf{E}(-\omega) \times \mathbf{E}(\omega) \equiv \mathbf{E}^*(\omega) \times \mathbf{E}(\omega) = 0$, while those of circularly polarized light satisfy $\mathbf{E}(-\omega) \times \mathbf{E}(\omega) \equiv \mathbf{E}^*(\omega) \times \mathbf{E}(\omega)$ is purely imaginary, we introduce the following definitions for LPGE and CPGE:

$$L_{\alpha_1\alpha_2}(\omega) = \text{Re} \{ E_{\alpha_1}^*(\omega) E_{\alpha_2}(\omega) \}, \quad (40)$$

$$\mathbf{F}(\omega) = \frac{1}{2} i \mathbf{E}^*(\omega) \times \mathbf{E}(\omega), \quad (41)$$

$$\eta_{\alpha_1\alpha_2}^{c/s_{\gamma},\beta}(\omega) = \frac{1}{2} \text{Re} \left(\sigma_{\alpha_1\alpha_2}^{c/s_{\gamma},\beta}(-\omega, \omega) + \sigma_{\alpha_2\alpha_1}^{c/s_{\gamma},\beta}(\omega, -\omega) \right), \quad (42)$$

$$\kappa_{\lambda}^{c/s_{\gamma},\beta}(\omega) = \frac{\epsilon_{\alpha_1\alpha_2\lambda}}{2} \text{Im} \left(\sigma_{\alpha_1\alpha_2}^{c/s_{\gamma},\beta}(-\omega, \omega) + \sigma_{\alpha_2\alpha_1}^{c/s_{\gamma},\beta}(\omega, -\omega) \right), \quad (43)$$

where $\epsilon_{\alpha_1\alpha_2\lambda}$ is Levi-Civita symbol. We note that $L_{\alpha_1\alpha_2}(\omega) \equiv L_{\alpha_2\alpha_1}(\omega)$ and $\eta_{\alpha_1\alpha_2}^{c/s_{\gamma},\beta} \equiv \eta_{\alpha_2\alpha_1}^{c/s_{\gamma},\beta}$. Here we call $\eta_{\alpha_1\alpha_2}^{c/s_{\gamma},\beta}$ ($\kappa_{\lambda}^{c/s_{\gamma},\beta}$) LPGE (CPGE) coefficient/susceptibility.

For LPGE, $\mathbf{F}(\omega) = 0$, so that only the real parts of $\sigma_{\alpha_1\alpha_2}^{c/s_{\gamma},\beta}(\mp\omega, \pm\omega)$ contribute. For CPGE, both the imaginary and real parts of $\sigma_{\alpha_1\alpha_2}^{c/s_{\gamma},\beta}(\mp\omega, \pm\omega)$ can contribute, as $\mathbf{F}(\omega) \neq 0$ and some of $L_{\alpha_1\alpha_2}(\omega)$ can be nonzero.

Using the relation

$$\sigma_{\alpha_1\alpha_2}^{c/s_{\gamma},\beta}(-\omega, \omega) = \left[\sigma_{\alpha_1\alpha_2}^{c/s_{\gamma},\beta}(\omega, -\omega) \right]^*, \quad (44)$$

the second-order dc current density for photon-frequency ω can be expressed as

$$\begin{aligned} J_{\beta}^{s_{\gamma}}(0) &= \sum_{\alpha_1\alpha_2\pm} E_{\alpha_1}(\mp\omega) E_{\alpha_2}(\pm\omega) \sigma_{\alpha_1\alpha_2}^{c/s_{\gamma},\beta}(\mp\omega, \pm\omega) \\ &= 2 \left\{ \sum_{\alpha_1\alpha_2} L_{\alpha_1\alpha_2}(\omega) \eta_{\alpha_1\alpha_2}^{c/s_{\gamma},\beta}(\omega) \right. \\ &\quad \left. + \sum_{\lambda} F_{\lambda}(\omega) \kappa_{\lambda}^{c/s_{\gamma},\beta}(\omega) \right\}. \end{aligned} \quad (45)$$

For CPGE, in many cases, $\kappa_{\lambda}^{c/s_{\gamma},\beta}$ are found much larger than $\eta_{\alpha_1\alpha_2}^{c/s_{\gamma},\beta}$, so that $\eta_{\alpha_1\alpha_2}^{c/s_{\gamma},\beta}$ are often not considered.

Let's consider a few special cases below:

(i) Suppose $\mathbf{E}(\omega) = E(1, 1, 0)$ with E a real value for a linearly polarized light. As $\mathbf{F}(\omega) = 0$, we have

$$J_\beta^{s_\gamma}(0) = 2 \sum_{\alpha_1, \alpha_2 = x, y} \eta_{\alpha_1 \alpha_2}^{c/s_\gamma, \beta} L_{\alpha_1 \alpha_2}(\omega). \quad (46)$$

(ii) Suppose $\mathbf{E}(\omega) = E(1, i, 0)$ with E a real value for a circularly polarized light. As $L_{xy}(\omega) = 0$ and $\mathbf{F}(\omega) = E^2(0, 0, -1)$, we have

$$J_\beta^{s_\gamma}(0) = 2 \left(\sum_{\alpha = x, y} L_{\alpha\alpha}(\omega) \eta_{\alpha\alpha}^{c/s_\gamma, \beta} + F_z(\omega) \kappa_z^{c/s_\gamma, \beta} \right). \quad (47)$$

D. Wannier interpolation and the computation of the covariant derivative $\frac{D\rho}{D\mathbf{k}}$

The Wannier interpolation based on maximally localized Wannier functions of electronic and electronic scattering quantities has been widely employed to simulate various physical properties.[29–34] The Wannier interpolation contains four steps: (i) The electronic and electronic scattering quantities are first calculated on coarse wavevector (k- or q-point) meshes, e.g., $6 \times 6 \times 6$ and 12×12 for 3D and 2D systems respectively. (ii) Secondly, they are transformed to the corresponding real-space matrix elements with (real-space) localized Wannier functions (WFs) as basis. (iii) Thirdly, physical quantities are transformed back to the reciprocal space. At this step, quantities on very fine wavevector meshes (e.g., 2000×2000) or at many arbitrary wavevectors in Wannier representation are obtained. In Wannier representation, the basis are the smooth Bloch-like functions described below. (iv) Finally, Wannier representation is replaced by the eigenbasis representation where the basis are the Bloch eigenstates of the Wannier-interpolated Hamiltonian. Thus, physical properties can be conveniently calculated with quantities in the eigenbasis representation with converged number of wavevectors.

In this subsection, different representations are used to express electronic quantities. Therefore, for clarity, no additional notation or superscript is used for the eigenbasis representation, while superscript W is used for the Wannier representation. Note that all equations above this subsection use the eigenbasis representation.

1. Wannier representation and Wannier interpolation

The WFs are noted as $|\mathbf{R}a\rangle$, where a is the index of a WF in the unitcell and \mathbf{R} labels the unitcell. The smooth Bloch-like functions are given by the phased sum of WFs

$$|u_{ka}^W\rangle = \sum_{\mathbf{R}} e^{-i\mathbf{k} \cdot (\mathbf{r} - \mathbf{R})} |\mathbf{R}a\rangle, \quad (48)$$

which span the actual Bloch eigenstates $|u_{ka}\rangle$ at each \mathbf{k} . It follows that, if we construct the Hamiltonian in the Wannier representation

$$H_{kab}^W = \langle u_{ka}^W | \hat{H}_k | u_{kb}^W \rangle \quad (49)$$

and diagonalize it as

$$U_k^\dagger H_k^W U_k = \epsilon_k, \quad (50)$$

where U_k are the eigenstate matrix and ϵ_k is the diagonal matrix of eigenvalues. The corresponding Bloch eigenstates are

$$|u_{ka}\rangle = \sum_b |u_{kb}^W\rangle U_{kba}. \quad (51)$$

Similar to H_k^W , the velocity and spin matrices are well defined in Wannier representation and are noted as \mathbf{v}_k^W and \mathbf{s}_k^W respectively. The computations of H_k^W , \mathbf{v}_k^W and \mathbf{s}_k^W are efficient and done through standard techniques developed in Ref. 30. With U_k , the velocity and spin matrices in the eigenbasis representation read

$$\mathbf{v}_k = U_k^\dagger \mathbf{v}_k^W U_k, \quad (52)$$

$$\mathbf{s}_k = U_k^\dagger \mathbf{s}_k^W U_k. \quad (53)$$

Having \mathbf{v}_k and \mathbf{s}_k , j_β^{c/s_γ} is obtained straightforwardly from Eq. 2 and 4. As the basis size of Wannier representation is usually small (same as the eigenbasis representation), the computations of ϵ_k , U_k , \mathbf{v}_k and \mathbf{s}_k are all efficient. The computational technique of Berry connection in Wannier representation ξ_k^W is slightly different from that of H_k^W and is also efficient.[30]

In previous *ab initio* methods of the photocurrent based on Wannier function,[16–20] it is often necessary to compute ξ_k (as the covariant derivative $\frac{D\rho}{D\mathbf{k}}$, defined in Eq. 8, involves ξ), which is expressed as

$$\xi_k = i\mathbf{D}_k + \bar{\xi}_k, \quad (54)$$

$$\mathbf{D}_k = U_k^\dagger \frac{dU_k}{d\mathbf{k}}, \quad (55)$$

$$\bar{\xi}_k = U_k^\dagger \xi_k^W U_k, \quad (56)$$

$$\xi_{kab}^W = i \left\langle u_{ka}^W \left| \frac{du_{kb}^W}{d\mathbf{k}} \right. \right\rangle. \quad (57)$$

However, computing \mathbf{D}_k directly via Eq. 55 is non-trivial and usually done using non-degenerate perturbation theory,[16, 30]

$$\mathbf{D}_{kab} \approx \mathbf{D}_{kab}^{\text{pert}}, \quad (58)$$

$$\mathbf{D}_{kab}^{\text{pert}} = \begin{cases} \left(U_k^\dagger \frac{dU_k^W}{d\mathbf{k}} U_k \right)_{ab}, & \text{if } \epsilon_{ka} \neq \epsilon_{kb} \\ 0, & \text{if } \epsilon_{ka} = \epsilon_{kb} \end{cases}. \quad (59)$$

Obviously, $\mathbf{D}_{kab}^{\text{pert}}$ is problematic for degenerate bands. This issue may be removed for two-fold degeneracy by

choosing a specific gauge of U_k , [35] but computing \mathbf{D}_{kab} for arbitrarily degenerate bands without an approximation is still difficult. This degeneracy issue is completely removed in our method, since \mathbf{D}_{kab} is absent in the computation of $\frac{D\rho}{D\mathbf{k}}$, as present clearly in the next subsection.

2. The computation of the covariant derivative $\frac{D\rho}{D\mathbf{k}}$

$\frac{D\rho}{D\mathbf{k}}$ is called the covariant derivative because it satisfies the following relation for arbitrary U :

$$\frac{D\rho}{D\mathbf{k}} = U^\dagger \frac{D\rho^W}{D\mathbf{k}} U, \quad (60)$$

where $\rho^W = U\rho U^\dagger$. The proof is given in Appendix B. Since

$$\frac{D\rho^W}{D\mathbf{k}} = \frac{d\rho^W}{d\mathbf{k}} - i[\xi^W, \rho^W], \quad (61)$$

we further have

$$\frac{D\rho}{D\mathbf{k}} = U^\dagger \frac{d\rho^W}{d\mathbf{k}} U - i[\bar{\xi}, \rho]. \quad (62)$$

Since the basis of Wannier representation u_{ka}^W is smooth over \mathbf{k} for each index a , the derivative $\frac{d\rho^W}{d\mathbf{k}}$ is well defined and can be computed numerically by finite difference. We use the central difference here. Define $\mathbf{k}_p = \mathbf{k} + d\mathbf{k}$ and $\mathbf{k}_m = \mathbf{k} - d\mathbf{k}$ so that

$$\begin{aligned} U_k^\dagger \frac{d\rho_k^W}{d\mathbf{k}} U_k &= U_k^\dagger \frac{\rho_{k_p}^W - \rho_{k_m}^W}{2d\mathbf{k}} U_k \\ &= \frac{\begin{pmatrix} U_k^\dagger U_{k_p} \rho_{k_p} U_{k_p}^\dagger U_k & \\ -U_k^\dagger U_{k_m} \rho_{k_m} U_{k_m}^\dagger U_k & \end{pmatrix}}{2d\mathbf{k}}. \end{aligned} \quad (63)$$

Define the overlap matrix

$$o_{k_1 k_2} = U_{k_1}^\dagger U_{k_2}, \quad (64)$$

we have

$$U_k^\dagger \frac{d\rho_k^W}{d\mathbf{k}} U_k = \frac{\begin{pmatrix} o_{kk_p} \rho_{k_p} o_{kk_p}^\dagger & \\ -o_{kk_m} \rho_{k_m} o_{kk_m}^\dagger & \end{pmatrix}}{2d\mathbf{k}}. \quad (65)$$

Due to the use of WF, electronic quantities including $\rho_k^{(n)}$ can be computed at arbitrary \mathbf{k} . Therefore, $|d\mathbf{k}|$ can be arbitrarily small and is typically chosen as 10^{-8} , which guarantees the accuracy of finite difference computations.

With Eq. 65 and $\bar{\xi}$ computed by Eq. 56, $\frac{D\rho}{D\mathbf{k}}$ is then obtained from Eq. 62. For numerical implementation of Eq. 65, helpful techniques are employed as described in Appendix C and D.

III. COMPUTATIONAL DETAILS

The ground-state electronic structure is first calculated using DFT with relatively coarse \mathbf{k} meshes. The DFT calculations use $12 \times 12 \times 12$, 12×12 and $6 \times 6 \times 6$ \mathbf{k} meshes for GaAs, 2D materials and RhSi respectively. We use Perdew-Burke-Ernzerhof exchange-correlation functional [36]. For bilayer AFM MBT, the DFT+U method is adopted to treat the d orbitals of Mn atoms with Hubbard U parameter 4.0 eV, and its lattice structures and internal geometries are fully relaxed using the DFT+D3 correction method [37] for dispersion interactions. For graphene-hBN, the DFT+D2 correction method [38] with scale factor $s_6 = 0.5$ is used to be consistent with our previous work [39]. For 3D and monolayer materials, van der Waals corrections are not important and not considered. For GaAs, we use the experimental lattice constant of 5.653 Å in our previous work [26]. For RhSi, we use experimental lattice constant [40] of 4.67 Å. For WS₂ and GeS, we use the fully relaxed lattice constants. We use Optimized Norm-Conserving Vanderbilt (ONCV) pseudopotentials [41, 42]. The plane-wave cutoff energies are 76, 74, 62, 44, 82 and 80 Ry for GaAs, graphene-hBN, WS₂, GeS, MBT and RhSi respectively. For all 2D systems, the Coulomb truncation technique [43] is employed to accelerate convergence with vacuum sizes and the vacuum sizes are 20 bohr (additional to the thickness of the heterostructures).

We then transform all quantities from plane-wave ba-

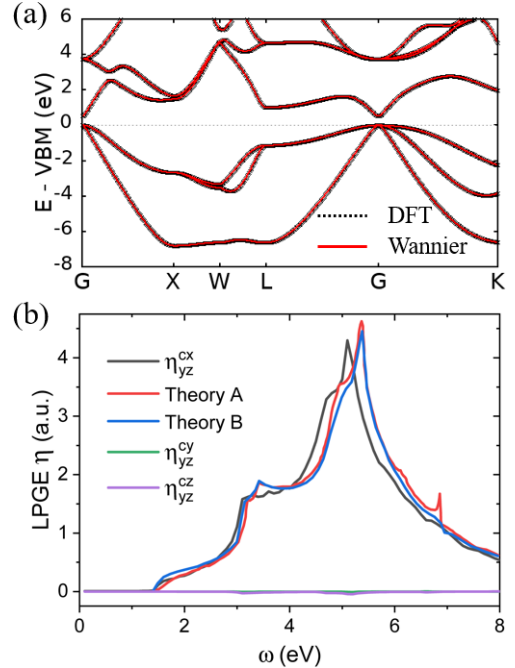


FIG. 1. Theoretical results of GaAs. (a) DFT and Wannier band structures. (b) LPGE coefficients $\eta_{\alpha_1 \alpha_2}^{c\beta}$ compared with η_{yz}^{cy} from previous theoretical results. “Theory A” and “Theory B” correspond to Refs. 16 and 44 respectively. A scissor correction is included as in Refs. 16 and 44.

sis to maximally localized Wannier function basis, and interpolate them to substantially finer k meshes.[29, 30] For the photocurrent calculations, the fine k meshes are $960 \times 960 \times 960$, 12000×12000 , 2400×2400 , 2400×2400 , 960×960 and $120 \times 120 \times 120$ for GaAs, graphene-hBN, WS₂, GeS, MBT and RhSi respectively. For simplicity, the elements of the relaxation rate matrices Γ_k are all set to the same constant, which unless specified is 0.001 eV/ \hbar for graphene-hBN and 0.01 eV/ \hbar for other materials, corresponding to a relaxation time of 666 and 66 fs respectively. All calculations are done based on the open-source plane-wave DFT code JDFTx[45–48].

IV. RESULTS AND DISCUSSIONS

Before presenting our theoretical results, we would like to clarify two points: (i) We simulate the photocurrent within RTA, so that the ballistic current is absent. (ii) The signs of optical susceptibilities and LPGE/CPGE coefficients depend on the definitions of x , y , z directions. For CPGE, the sign of $\kappa_\lambda^{c/s\gamma,\beta}$ depends on the definition of $\mathbf{F}(\omega)$. Therefore, when comparing with other theoretical works, we should be careful about these definitions.

A. First benchmark: GaAs

GaAs is a typical semiconductor with broken inversion symmetry, which allows the presence of the second-order photocurrent - BPVE and SHG. Due to its symmetry, LPGE of GaAs is allowed while CPGE not. Without considering the ballistic current, LPGE of GaAs is determined by shift current. GaAs was the first piezoelectric crystal whose shift-current spectrum was evaluated using modern band structure methods[49] and later simulated in other method papers[16, 44]. Therefore, we first carry out benchmark calculations of LPGE of GaAs.

In Fig. 1(a), we compare DFT and Wannier band structures and find that they agree perfectly. This ensures the accuracy of the photocurrent calculation based on Wannier function. From symmetry analysis, it is known that LPGE coefficient $\eta_{\alpha_1\alpha_2}^{c\beta}$ are only non-zero for permutations $\beta\alpha_1\alpha_2$ of xyz . Indeed, in Fig. 1(b), numerically we find that $\eta_{yz}^{cx} \neq 0$ while η_{yz}^{cy} and η_{yz}^{cz} almost vanish. Our calculated η_{yz}^{cx} are in good agreement with previous theoretical results[16, 44], which indicates the reliability of the implementation of our method.

B. A 2D material: LPGE and LHG of graphene-hBN

Since the discovery of graphene, low-frequency nonlinear optical response of graphene has attract lots of attention of both theorists and experimentalists.[8, 13, 50–53] Here we simulate low-order optical susceptibilities of graphene-hBN. The hBN substrate is introduced to

break the inversion symmetry to allow non-zero LPGE and SHG.

Three types of photocurrent simulations using three types of electronic Hamiltonian H^0 are carried out:

(i) “TB”: Minimum tight-binding Hamiltonian (as in Ref. 53) with two atomic orbitals (in the unitcell) and two energy parameters - gap $E_g=0.0416$ eV (same as our DFT value) and a nearest-neighbor hopping parameter $t=2.8$ eV. A t around 2.8 eV has been commonly used to model graphene. Note that if choosing $E_g=0.03$ eV as in Ref. 53, we can reproduce their LPGE and LHG spectra;

(ii) “Wannier A”: Minimum *ab initio* Wannier-interpolated Hamiltonian with two WFs (in the unitcell), which reproduces DFT eigenvalues within the energy window $[E_F-1$ eV, E_F+3 eV]. From Fig. 2(a), it can be seen that “Wannier A” nicely reproduces DFT bands with tiny errors around Dirac cones;

(iii) “Wannier B”: *ab initio* Wannier-interpolated Hamiltonian with 20 WFs, which reproduces DFT eigenvalues within $[E_F-6$ eV, $E_F+7.7$ eV]. From Fig. 2(a), it can be seen that “Wannier B” perfectly reproduces DFT bands.

From Fig. 2(b)-(d), we find that “Wannier A” and “Wannier B” results of LPGE, SHG and THG susceptibilities are identical, and TB leads to similar results. The curves of TB results have the same shapes as *ab initio* results based on Wannier function, and the ratios of TB results to *ab initio* results range from 63% to 123%, which are insignificant. Therefore, our results indicate that a minimum TB model and a minimum Wannierization setup are good enough for simulations of LPGE and LHG (within RTA) of graphene-hBN. This conclusion however may not applicable if band structures are complicated and/or spin-orbit coupling plays a crucial role, in which cases sophisticated *ab initio* Wannierization setups are required. Additionally, it is found that TB results are insensitive to the nearest-neighbor hoping parameter t (not shown), so that to cure the differences between TB and *ab initio* results, farther-neighbor hoppings are probably needed.

We next investigate the response of different photon processes for low-frequency LPGE and LHG of the semi-conducting graphene-hBN. From Fig. 2(b), the LPGE spectrum shows a one-photon resonant peak - a peak right above $\omega = E_g$. This is consistent with the fact that the formula of LPGE susceptibility contains a delta-like function $d_{kab}^\Gamma(1\omega)$ (according to Eq. 32, 34 and 35), which has a resonant energy at $\omega = \Delta_{kab}$. For SHG shown in Fig. 2(c), it is found that its spectrum shows three peaks - two one-photon resonant peaks around $\omega = E_g$ and one two-photon resonant peak right above $2\omega = E_g$. This is because the formula of SHG susceptibility (Eq. 37, 36 and 32) contains both $d^\Gamma(2\omega)$ and $d^\Gamma(1\omega)$. For THG, its spectrum (Fig. 2(d)) has a sharp three-photon resonant peak right above $3\omega = E_g$ corresponding to $d^\Gamma(3\omega)$ in the formula of THG (Eq. 39, 38, 36 and 32). On the other hand, the THG spectrum shows less clear features for two-photon processes and

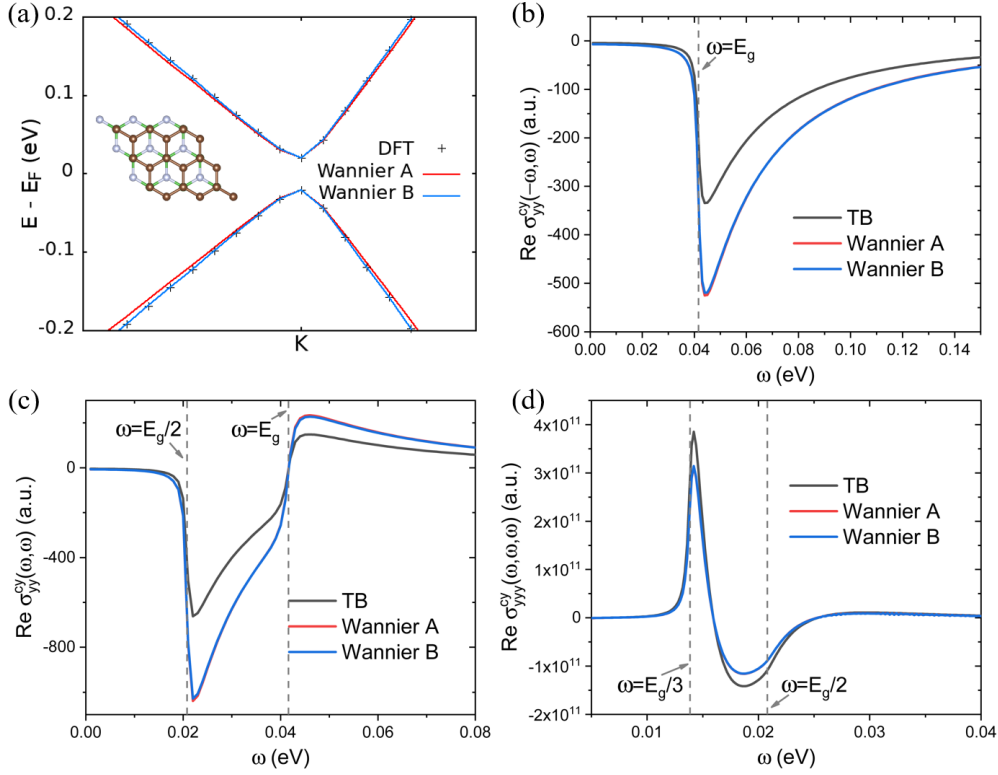


FIG. 2. Theoretical results of graphene-hBN. (a) DFT and Wannier band structures. “Wannier A” and “Wannier B” mean Wannier-interpolated Hamiltonians with 2 and 20 WFs (in the unitcell) respectively. (b), (c) and (d) are optical susceptibilities of LPGE ($\text{Re} \sigma_{yy}^{cy}(\omega, \omega, \omega)$), SHG ($\text{Re} \sigma_{yy}^{cy}(\omega, \omega)$) and THG ($\text{Re} \sigma_{yy}^{cy}(-\omega, \omega)$) respectively calculated using three types of Hamiltonians - a two-band tight-binding (TB) Hamiltonian, “Wannier A” and “Wannier B”. See more details of TB, “Wannier A” and “Wannier B” in the text of Sec. IV B. Three special photon energies satisfying $\omega, 2\omega, 3\omega = E_g$, corresponding to one-, two-, three-photon processes respectively, are labeled in (b), (c) and (d) using vertical dashed lines.

no obvious features for one-photon processes: (i) The second peak of the THG spectrum is a bit away from $2\omega = E_g$ and relatively broad; (ii) THG susceptibilities around $\omega = E_g$ are much weaker than its maximum value.

C. A 2D material: (Spin) LPGE of monolayer WS_2

Besides graphene, transition metal dichalcogenides (TMDs) are another important class of 2D materials. Optical (spin-)current generation is critical to the TMD-based electronic and spintronic applications and has been extensively studied experimentally and theoretically.[12, 17, 54–56]

Here we study both LPGE and spin LPGE (SLPGE) of monolayer 2H WS_2 . As shown in Fig. 3(b), a high-quality Wannierization is achieved, which ensures the accuracy of our *ab initio* simulations. We first investigate the effects of SOC on LPGE susceptibilities. From Fig. 3(c), our calculated LPGE spectrum is in good agreement with previous theoretical results[17] and the SOC effects are found significant. Most importantly, the first peak near $\omega = E_g$ of the LPGE spectrum without SOC is splitted to two by SOC (labeled as “V1” and “V2” in Fig. 3(c)), and the splitting of two peaks is close to the

SOC band splitting between two highest valence bands at \mathbf{K} , ~ 0.43 eV.

Therefore, we include SOC in further *ab initio* simulations of LPGE and SLPGE susceptibilities of monolayer WS_2 , shown in Fig. 3(d) and (e). Note that spin current is only present when SOC is turned on. We find that charge and spin currents are perpendicular to each other - charge current is along y direction while spin current is along x direction under linearly polarized light. This means a pure spin current (along x direction) is generated by SLPGE. This phenomenon is due to the different selection rule on charge and spin currents in the presence of in-plane mirror symmetry $\mathcal{M}_x: k_x \rightarrow -k_x$ for non-magnetic 2D TMDs.[12]

D. A 2D material: LPGE and CPGE of 2D ferroelectric GeS

Recently, ferroelectric group-IV monochalcogenide monolayers have attract growing interests due to their exciting properties, such as selective valley excitations, valley Hall effects, and persistent spin helix behavior.[57] They also show interesting nonlinear optical properties including an unusually strong SHG intensity, large

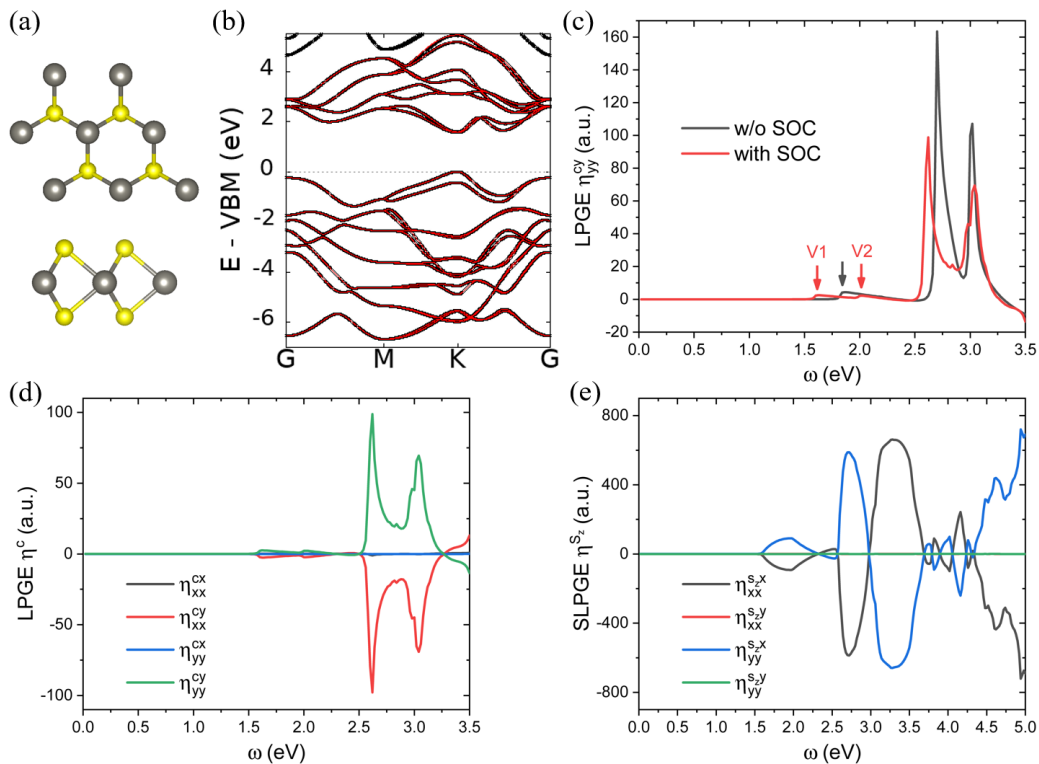


FIG. 3. Theoretical results of monolayer WS₂. (a) Top and side views of the structure. (b) DFT (black lines) and Wannier (red lines) band structures. (c) LPGE susceptibilities η_{yy}^{cy} with and without spin-orbit coupling (SOC). (d) LPGE susceptibilities with SOC for different electric field and current directions. (e) Spin LPGE (SLPGE) susceptibilities with SOC.

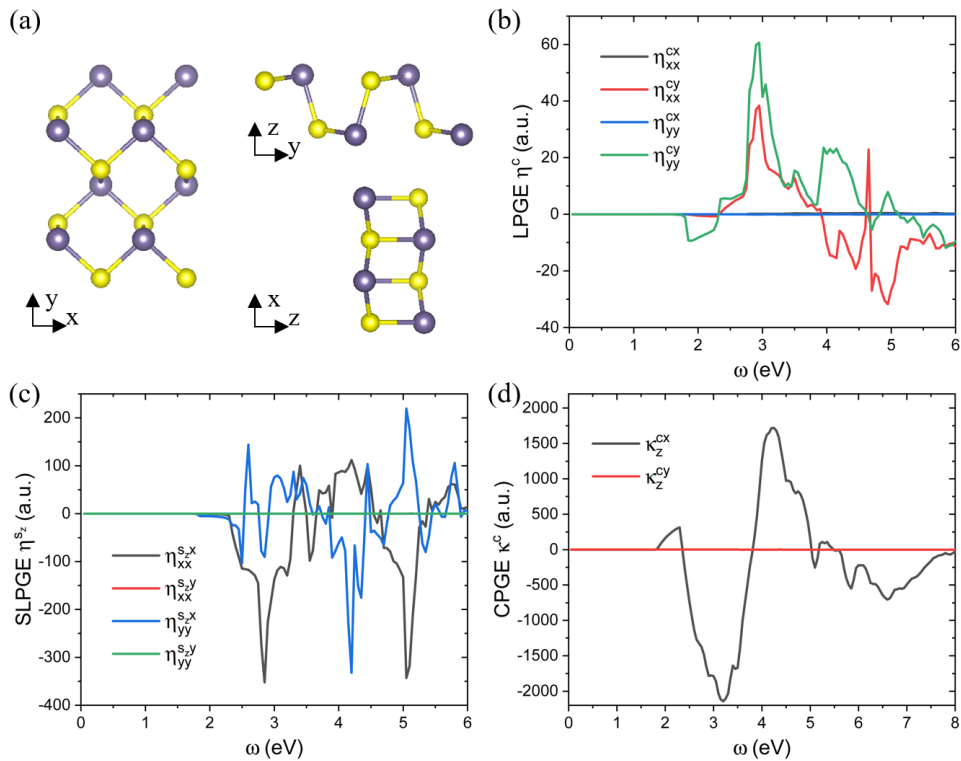


FIG. 4. Theoretical results of monolayer GeS. (a) Top and side views of the structure. Calculated (b) LPGE (c) SLPGE and (d) CPGE susceptibilities. SOC is considered.

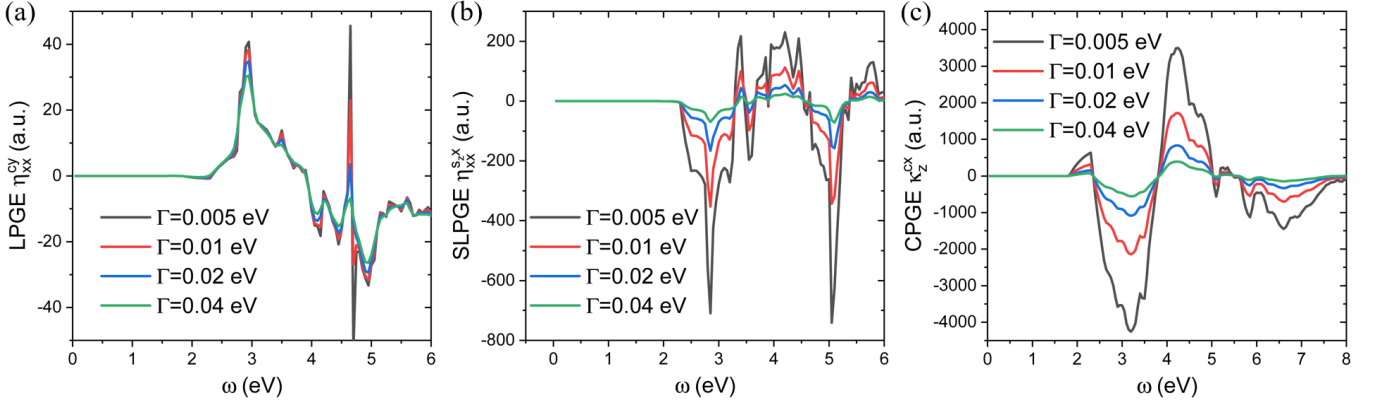


FIG. 5. Relaxation rate Γ dependence of calculated (a) LPGE, (b) SLPGE and (d) CPGE susceptibilities.

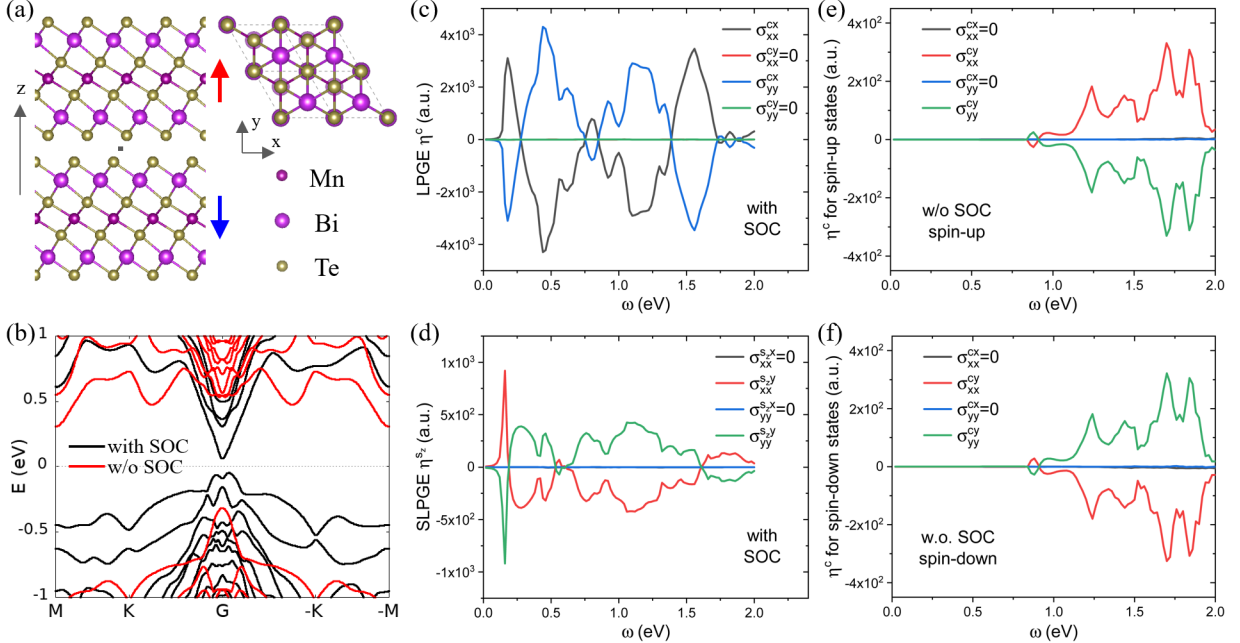


FIG. 6. Theoretical results of bilayer AFM MBT. (a) Side and top views of its crystal structure. This system has both inversion symmetry \mathcal{P} and mirror symmetry \mathcal{M}_z : $z \rightarrow -z$. This inversion center is in between two layers (black square). Red and blue arrows indicate the magnetic moment directions of the top and bottom MBT layers respectively. The system has the so-called \mathcal{PT} symmetry, i.e., the system is invariant if inversion operation \mathcal{P} and time-reversal operation \mathcal{T} are applied together. (b) Band structures with (black lines) and without (red lines) SOC. (c) and (d) are calculated LPGE and SLPGE susceptibilities with SOC respectively. (e) and (f) are calculated LPGE susceptibilities for spin-up and spin-down states without SOC respectively.

BPVE.[57]

Here we study LPGE, SLPGE and CPGE of a group-IV monochalcogenide monolayer - monolayer GeS. Our results shown in Fig. 4 are in good agreement with previous theoretical ones[58, 59]. Similar to monolayer WS₂, from Fig. 4(b) and (c), we find pure spin currents perpendicular to charge currents, which is again due to the presence of in-plane mirror symmetry \mathcal{M}_x : $k_x \rightarrow -k_x$. Further, we observe strong CPGE (Fig. 4(d)), 30 times stronger than LPGE. According to previous theoretical works[2, 21, 59], as monolayer GeS is nonmagnetic, its CPGE is mainly attributed to the injection current,

where the DC photocurrent is determined by the inter-band parts of $\frac{D\rho^{(n)}}{D\mathbf{k}}$ (Appendix A) and the intra-band part of the current operator $\mathbf{j}^{c/s\gamma}$. Strong CPGE due to injection current has been predicted in ferroelectric group-IV monochalcogenide monolayers including GeS, GeSe, SnS and SnSe, and it is attributed to various factors in these materials such as anisotropy, in-plane polarization and wave function delocalization.[59]

It is well known that optical susceptibilities due to injection current are proportion to relaxation time $\tau = 1/\Gamma$ if $\Gamma > 0$.[21] Therefore, we next examine the Γ dependence of susceptibilities of CPGE as well as LPGE and

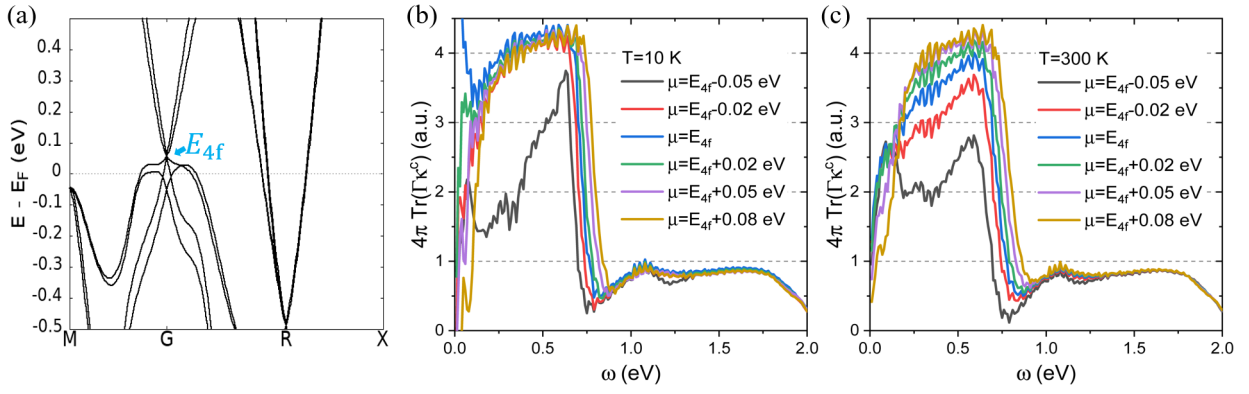


FIG. 7. Theoretical results of RhSi with SOC. (a) Band structure. E_{4f} is the energy of the four-fold degenerate point. (b) and (c) are traces of CPGE susceptibilities κ^c multiplied by a factor of $4\pi\Gamma$ at different chemical potentials μ at 10 K and 300 K respectively.

SLPGE. From Fig. 5(a), it is found that LPGE is independent from Γ except delta-like features around 4.6 eV. This is because LPGE of a nonmagnetic semiconducting material such as monolayer GeS should be dominated by the shift current contribution, which is known independent from Γ . [2, 21] Calculated CPGE susceptibilities κ^c are found proportional to $1/\Gamma$ (Fig. 5(c)) as expected. Calculated SLPGE susceptibilities η^{sz} are found proportional to $1/\Gamma$ (Fig. 5(d)), which is probably because SLPGE is also dominated by the injection current (the same as CPGE) as discussed in Ref. 60.

E. A magnet: Bilayer AFM MBT

Recently, various exotic BPVE properties have been predicted for AFM systems with the so-called \mathcal{PT} symmetry, which means the systems are invariant if inversion operation \mathcal{P} and time-reversal operation \mathcal{T} are applied together. [7, 12, 21] Here we apply our method to simulate LPGE and SLPGE of bilayer AFM MBT, which has the \mathcal{PT} symmetry. Similar to Ref. 12, we have the following observations from Fig. 6: (i) SOC affects both band structure and BPVE significantly; (ii) Pure spin currents are present regardless of SOC. This is due to the different selection rule on charge and spin- z currents in the presence of the \mathcal{PM}^x symmetry. [12] (iii) With SOC, the charge current is present (see Fig. 6(b)) and perpendicular to spin- z current (see Fig. 6(d)). However, without SOC, the charge current, which is the sum of the spin-up and spin-down currents, is absent (see Fig. 6(e) and (f)). This is because the so-called inversion-spin-rotation \mathcal{PS} symmetry is satisfied without SOC but is broken if SOC is turned on, according to Ref. 12.

F. A topological Weyl semimetal: Quantized CPGE in RhSi

CPGE serves as an invaluable tool to detect the chirality, topological charge, symmetries and other properties of topological Weyl semimetals. [4, 5, 11, 19] Previously, quantized CPGE has been studied theoretically considering only the injection current contribution, and via model Hamiltonians [4] or Wannier-function-based *ab initio* methods with the so-called diagonal tight-binding approximation (DTBA) [11, 19], in which ξ^W is treated approximately [16].

The so-called quantized-CPGE suggests that the relation: $\text{Tr}[\beta(\omega)] = i\pi \frac{e^3}{h^2} C_L$ with C_L topological charge, is satisfied in a certain photon-frequency range. [4, 19] For the injection current (which dominates quantized CPGE) with a finite relaxation time $\tau = 1/\Gamma$, there is $\beta(\omega) = i\Gamma\kappa^c(\omega)$. [2, 21] Therefore, the quantized-CPGE relation becomes: $4\pi\text{Tr}[\Gamma\kappa^c] = C_L$ in atomic units.

In this work, we apply our *ab initio* method to simulate CPGE of RhSi at various temperatures and chemical potentials μ . We have gone beyond DTBA and considered photocurrent contributions beyond just the injection current. From our calculated CPGE spectra in Fig. 7, we observe that $4\pi\text{Tr}[\Gamma\kappa^c(\omega)] \approx 4$ in a relatively wide photon-energy range [0.3, 0.6] eV at both low (Fig. 7(b)) and high (Fig. 7(c)) temperatures, if μ is not too low. Our results suggest that it seems easier to observe quantized CPGE at lower temperatures and higher μ .

V. SUMMARY AND OUTLOOKS

We have developed an *ab initio* method based on Wannier function for simulating weak-field BPVE and LHG in solids. The method is of great predictive power and widely applicable to semiconductors and metals with arbitrary band structures for both linearly and circularly polarized light. We demonstrated its power through its applications into the simulations of (S)LPGE, (S)CPGE

and LHG in various types of systems.

This method has the potential to be greatly improved in various directions, such as: (i) By introducing a static electric field, which can be done straightforwardly, the so-called jerk current[61] can be simulated. (ii) The scattering term within RTA with a global constant relaxation time $\tau = 1/\Gamma$ can be replaced by the fully *ab initio* sophisticated scattering terms developed in our previous works[26, 27], so that the energy-, \mathbf{k} - and transition-resolved relaxation and decoherence are accurately considered. This generation may have important effects on quantized CPGE, which is predicted within RTA with a global τ . (iii) By solving the density matrix non-perturbatively via real-time dynamics, the photocurrent at stronger fields can be simulated.

ACKNOWLEDGEMENTS

Junqing Xu thanks Ravishankar Sundararaman for helpful discussions. This work is supported by National Natural Science Foundation of China (Grant No. 12304214 and No. 12104122), Fundamental Research Funds for Central Universities (Grant No. JZ2023HGPA0291), Anhui Provincial Natural Science Foundation (Grant No. 1908085QA16). This research used resources of the HPC Platform of Hefei University of Technology.

APPENDICES

Appendix A: Intra- and inter-band parts of $\frac{D\rho}{D\mathbf{k}}$

$\frac{D\rho}{D\mathbf{k}}$ can be separated into the intra- and inter-band parts

$$\frac{D\rho}{D\mathbf{k}} = \left(\frac{D\rho}{D\mathbf{k}}\right)^{\text{intra}} + \left(\frac{D\rho}{D\mathbf{k}}\right)^{\text{inter}}, \quad (66)$$

$$\left(\frac{D\rho}{D\mathbf{k}}\right)^{\text{intra}} = \frac{d\rho}{d\mathbf{k}} - i [\xi^{\text{intra}}, \rho], \quad (67)$$

$$\left(\frac{D\rho}{D\mathbf{k}}\right)^{\text{inter}} = -i [\xi^{\text{inter}}, \rho], \quad (68)$$

$$\xi_{kab}^{\text{intra}} = \delta_{\epsilon_{ka}\epsilon_{kb}} \xi_{kab}, \quad (69)$$

$$\begin{aligned} \xi_{kab}^{\text{inter}} &= (1 - \delta_{\epsilon_{ka}\epsilon_{kb}}) \xi_{kab} \\ &= (1 - \delta_{\epsilon_{ka}\epsilon_{kb}}) \frac{\mathbf{v}_{kab}}{i\Delta_{kab}}. \end{aligned} \quad (70)$$

As ξ^{inter} can be easily obtained from \mathbf{v} , the computation of $\left(\frac{D\rho}{D\mathbf{k}}\right)^{\text{inter}}$ is straightforwardly. Then, since $\frac{D\rho}{D\mathbf{k}}$ can be computed by the method given in Sec. IID 2, $\left(\frac{D\rho}{D\mathbf{k}}\right)^{\text{intra}}$ can be obtained from $\left(\frac{D\rho}{D\mathbf{k}}\right)^{\text{intra}} = \frac{D\rho}{D\mathbf{k}} - \left(\frac{D\rho}{D\mathbf{k}}\right)^{\text{inter}}$.

Appendix B: The proof of Eq. 8

From $\rho^W = U\rho U^\dagger$ and Eq. 55 - $\mathbf{D} = U^\dagger \frac{dU}{d\mathbf{k}}$, we have

$$\begin{aligned} \frac{d\rho^W}{d\mathbf{k}} &= \frac{dU\rho U^\dagger}{d\mathbf{k}} \\ &= \frac{dU}{d\mathbf{k}}\rho U^\dagger + U\frac{d\rho}{d\mathbf{k}}U^\dagger + U\rho\frac{dU^\dagger}{d\mathbf{k}} \\ &= U\left(\frac{d\rho}{d\mathbf{k}} + \mathbf{D}\rho + \rho\mathbf{D}^\dagger\right)U^\dagger \\ &= U\left\{\frac{d\rho}{d\mathbf{k}} + [\mathbf{D}, \rho]\right\}U^\dagger. \end{aligned} \quad (71)$$

With Eq. 54 - $\xi = i\mathbf{D} + U^\dagger\xi^W U$, we then have,

$$\begin{aligned} \frac{D\rho}{D\mathbf{k}} &= \frac{d\rho}{d\mathbf{k}} - i[\xi, \rho] \\ &= \frac{d\rho}{d\mathbf{k}} - i[i\mathbf{D} + U^\dagger\xi^W U, \rho] \\ &= \frac{d\rho}{d\mathbf{k}} + [\mathbf{D}, \rho] - i[U^\dagger\xi^W U, \rho] \\ &= U^\dagger\frac{d\rho^W}{d\mathbf{k}}U - i[U^\dagger\xi^W U, U^\dagger\rho^W U] \\ &= U^\dagger\left(\frac{d\rho^W}{d\mathbf{k}} - -i[\xi^W, \rho^W]\right)U \\ &= U^\dagger\frac{D\rho^W}{D\mathbf{k}}U. \end{aligned} \quad (72)$$

Appendix C: The computation of $\frac{Df^{\text{eq}}}{D\mathbf{k}}$ without finite difference

From Eq. 3 and 10, we have

$$\begin{aligned} \mathbf{v}_{kab} &= \frac{1}{\hbar} \left(\frac{DH_k^0}{D\mathbf{k}}\right)_{ab} \\ &= \frac{1}{\hbar} \frac{d\epsilon_{ka}}{d\mathbf{k}} \delta_{ab} + \frac{i}{\hbar} \xi_{kab} \Delta_{kab}, \end{aligned} \quad (73)$$

so that

$$\xi_{ab} = -i \frac{\hbar \mathbf{v}_{kab}}{\Delta_{kab}}, \text{ if } \Delta_{kab} \neq 0. \quad (74)$$

Then, we have

$$\begin{aligned} -i[\xi_k, f_k^{\text{eq}}]_{ab} &= i\xi_{kab} (f_{ka}^{\text{eq}} - f_{kb}^{\text{eq}}) \\ &= i\xi_{kab} (f_{ka}^{\text{eq}} - f_{kb}^{\text{eq}}) (1 - \delta_{\epsilon_{ka}, \epsilon_{kb}}) \\ &= \hbar \mathbf{v}_{kab} \frac{f_{ka}^{\text{eq}} - f_{kb}^{\text{eq}}}{\epsilon_{ka} - \epsilon_{kb}} (1 - \delta_{\epsilon_{ka}, \epsilon_{kb}}). \end{aligned} \quad (75)$$

Therefore,

$$\left(\frac{Df_k^{\text{eq}}}{D\mathbf{k}}\right)_{ab} = \left(\frac{\Delta f^{\text{eq}}}{\Delta\epsilon}\right)_{kab} \hbar \mathbf{v}_{kab}, \quad (76)$$

$$\left(\frac{\Delta f^{\text{eq}}}{\Delta\epsilon}\right)_{kab} = \left(\frac{df_{ka}^{\text{eq}}}{d\epsilon}\right) \delta_{ab} \quad (77)$$

$$+ \frac{f_{ka}^{\text{eq}} - f_{kb}^{\text{eq}}}{\epsilon_{ka} - \epsilon_{kb}} (1 - \delta_{\epsilon_{ka}, \epsilon_{kb}}). \quad (78)$$

As $\frac{df_{ka}^{\text{eq}}}{d\epsilon} = (k_B T)^{-1} f_{ka}^{\text{eq}} (f_{ka}^{\text{eq}} - 1)$ can be evaluated analytically, numerical finite difference is avoid for the computation of $\frac{Df_{ka}^{\text{eq}}}{D\mathbf{k}}$. Numerically, we have found that computing $\frac{Df_{ka}^{\text{eq}}}{D\mathbf{k}}$ via Eq. 65 with finite difference and via Eq. 76 lead to almost the same results. Eq. 76 is preferred since it is computationally convenient.

Appendix D: The computation of $\bar{\xi}$ (Eq. 56)

The accuracy of $\bar{\xi}_k$ seems sometimes a bit worse when DFT meshes are not so dense, compared with H_k , \mathbf{v}_k and \mathbf{s}_k , whose accuracy is good even when DFT coarse k meshes for constructing WFs are quite coarse[29], e.g., $4 \times 4 \times 4$. [30] This is because: In usual implementation of ξ_k^W (Eq. 57, which determines $\bar{\xi}$) using the plane-wave DFT method, finite differences of u_k^W on DFT coarse meshes are required. Although u_k^W is smooth over \mathbf{k} , too coarse k meshes may still lead to some errors. This issue can be removed by increasing DFT k meshes or by using another implementation of ξ_k^W without finite difference.[30]

Here we introduce another technique to improve the accuracy of $\bar{\xi}$:

From Eq. 3, 10 and 65, we have

$$\begin{aligned} \mathbf{v}_{kab} &= \frac{1}{\hbar} \left(\frac{DH_k^0}{D\mathbf{k}} \right)_{ab} \\ &= \frac{1}{\hbar} U^\dagger \frac{dH^W}{d\mathbf{k}} U - \frac{i}{\hbar} [\bar{\xi}, \epsilon]. \end{aligned} \quad (79)$$

Therefore,

$$\bar{\xi}_{kab} = \frac{\hbar \mathbf{v}_{kab} - \left(U_k^\dagger \frac{dH_k^W}{d\mathbf{k}} U_k \right)_{ab}}{i \Delta_{kab}} \text{ if } \epsilon_{ka} \neq \epsilon_{kb}. \quad (80)$$

Since $\frac{dH^W}{d\mathbf{k}}$ can be computed accurately and efficiently without finite difference,[30] the computation of $\bar{\xi}_{kab}$ for the elements satisfying $\epsilon_{ka} \neq \epsilon_{kb}$ by Eq. 80 above is also accurate and efficient.

REFERENCE

-
- [1] V. Fridkin, *Crystallogr. Rep.* **46**, 654 (2001).
 - [2] Z. Dai and A. M. Rappe, *Chem. Phys. Rev.* **4** (2023).
 - [3] J. E. Spanier, V. M. Fridkin, A. M. Rappe, A. R. Akbasheshev, A. Polemi, Y. Qi, Z. Gu, S. M. Young, C. J. Hawley, D. Imbrenda, *et al.*, *Nat. Photonics* **10**, 611 (2016).
 - [4] F. De Juan, A. G. Grushin, T. Morimoto, and J. E. Moore, *Nat. Commun.* **8**, 15995 (2017).
 - [5] D. Rees, K. Manna, B. Lu, T. Morimoto, H. Borrmann, C. Felser, J. Moore, D. H. Torchinsky, and J. Orenstein, *Sci. Adv.* **6**, eaba0509 (2020).
 - [6] H. Yuan, X. Wang, B. Lian, H. Zhang, X. Fang, B. Shen, G. Xu, Y. Xu, S.-C. Zhang, H. Y. Hwang, *et al.*, *Nat. Nanotechnol.* **9**, 851 (2014).
 - [7] R. Fei, W. Song, L. Pusey-Nazzaro, and L. Yang, *Phys. Rev. Lett.* **127**, 207402 (2021).
 - [8] S.-Y. Hong, J. I. Dadap, N. Petrone, P.-C. Yeh, J. Hone, and R. M. Osgood Jr, *Phys. Rev. X* **3**, 021014 (2013).
 - [9] R. E. F. Silva, F. Martín, and M. Ivanov, *Phys. Rev. B* **100**, 195201 (2019).
 - [10] Y.-H. Chan, D. Y. Qiu, F. H. da Jornada, and S. G. Louie, *Proc. Natl. Acad. Sci. USA* **118**, e1906938118 (2021).
 - [11] F. de Juan, Y. Zhang, T. Morimoto, Y. Sun, J. E. Moore, and A. G. Grushin, *Phys. Rev. Res.* **2**, 012017(R) (2020).
 - [12] H. Xu, H. Wang, J. Zhou, and J. Li, *Nat. Commun.* **12**, 4330 (2021).
 - [13] G. Soavi, G. Wang, H. Rostami, D. G. Purdie, D. De Fazio, T. Ma, B. Luo, J. Wang, A. K. Ott, D. Yoon, *et al.*, *Nat. Nanotechnol.* **13**, 583 (2018).
 - [14] Z. H. Levine and D. C. Allan, *Phys. Rev. Lett.* **66**, 41 (1991).
 - [15] S. M. Young and A. M. Rappe, *Phys. Rev. Lett.* **109**, 116601 (2012).
 - [16] J. Ibañez-Azpiroz, S. S. Tsirkin, and I. Souza, *Phys. Rev. B* **97**, 245143 (2018).
 - [17] C. Wang, X. Liu, L. Kang, B.-L. Gu, Y. Xu, and W. Duan, *Phys. Rev. B* **96**, 115147 (2017).
 - [18] Y. Zhang, T. Holder, H. Ishizuka, F. de Juan, N. Nagaosa, C. Felser, and B. Yan, *Nat. Commun.* **10**, 3783 (2019).
 - [19] C. Le, Y. Zhang, C. Felser, and Y. Sun, *Phys. Rev. B* **102**, 121111(R) (2020).
 - [20] Y. Zhang, Y. Sun, and B. Yan, *Phys. Rev. B* **97**, 041101(R) (2018).
 - [21] H. Watanabe and Y. Yanase, *Phys. Rev. X* **11**, 011001 (2021).
 - [22] G. Ventura, D. Passos, J. L. dos Santos, J. V. P. Lopes, and N. Peres, *Phys. Rev. B* **96**, 035431 (2017).
 - [23] D. Passos, G. Ventura, J. V. P. Lopes, J. L. dos Santos, and N. Peres, *Phys. Rev. B* **97**, 235446 (2018).
 - [24] L. Yue and M. B. Gaarde, *Phys. Rev. A* **101**, 053411 (2020).
 - [25] Q. Sun, X. Xie, and J. Wang, *Phys. Rev. B* **77**, 035327 (2008).
 - [26] J. Xu, A. Habib, R. Sundararaman, and Y. Ping, *Phys. Rev. B* **104**, 184418 (2021).
 - [27] J. Xu and Y. Ping, *J. Chem. Theory Comput.* (2023).
 - [28] Z. Dai, A. M. Schankler, L. Gao, L. Z. Tan, and A. M. Rappe, *Phys. Rev. Lett.* **126**, 177403 (2021).
 - [29] N. Marzari, A. A. Mostofi, J. R. Yates, I. Souza, and D. Vanderbilt, *Rev. Mod. Phys.* **84**, 1419 (2012).
 - [30] X. Wang, J. R. Yates, I. Souza, and D. Vanderbilt, *Phys. Rev. B* **74**, 195118 (2006).
 - [31] J. Xu, K. Li, U. N. Huynh, M. Fadel, J. Huang, R. Sundararaman, V. Vardeny, and Y. Ping, *Nat. Commun.* **15**, 188 (2024).

- [32] J. Xu, A. Habib, S. Kumar, F. Wu, R. Sundararaman, and Y. Ping, *Nat. Commun.* **11**, 2780 (2020).
- [33] J. Xu, H. Takenaka, A. Habib, R. Sundararaman, and Y. Ping, *Nano Lett.* **21**, 9594 (2021).
- [34] J. Xu and Y. Ping, *npj Comput. Mater.* **9**, 47 (2023).
- [35] H. Chen, M. Ye, N. Zou, B.-L. Gu, Y. Xu, and W. Duan, *Phys. Rev. B* **105**, 075123 (2022).
- [36] J. P. Perdew, K. Burke, and M. Ernzerhof, *Phys. Rev. Lett.* **77**, 3865 (1996).
- [37] S. Grimme, J. Antony, S. Ehrlich, and H. Krieg, *J. Chem. Phys.* **132** (2010).
- [38] S. Grimme, *J. Comput. Chem.* **27**, 1787 (2006).
- [39] A. Habib, J. Xu, Y. Ping, and R. Sundararaman, *Phys. Rev. B* **105**, 115122 (2022).
- [40] S. Geller and E. Wood, *Acta Crystallogr.* **7**, 441 (1954).
- [41] D. R. Hamann, *Phys. Rev. B* **88**, 085117 (2013).
- [42] M. J. van Setten, M. Giantomassi, E. Bousquet, M. J. Verstraete, D. R. Hamann, X. Gonze, and G.-M. Rignanese, *Comput. Phys. Commun.* **226**, 39 (2018).
- [43] S. Ismail-Beigi, *Phys. Rev. B* **73**, 233103 (2006).
- [44] F. Nastos and J. E. Sipe, *Phys. Rev. B* **74**, 035201 (2006).
- [45] R. Sundararaman, K. Letchworth-Weaver, K. A. Schwarz, D. Gunceler, Y. Ozhaves, and T. Arias, *SoftwareX* **6**, 278 (2017).
- [46] A. M. Brown, R. Sundararaman, P. Narang, W. A. Goddard III, and H. A. Atwater, *ACS nano* **10**, 957 (2016).
- [47] A. Habib, F. Florio, and R. Sundararaman, *J. Opt.* **20**, 064001 (2018).
- [48] S. Kumar, C. Multunas, and R. Sundararaman, *Phys. Rev. Mater.* **6**, 125201 (2022).
- [49] J. E. Sipe and A. I. Shkrebtii, *Phys. Rev. B* **61**, 5337 (2000).
- [50] S. A. Mikhailov, *Europhys. Lett.* **79**, 27002 (2007).
- [51] T. Higuchi, C. Heide, K. Ullmann, H. B. Weber, and P. Hommelhoff, *Nature* **550**, 224 (2017).
- [52] Y. K. Luo, J. Xu, T. Zhu, G. Wu, E. J. McCormick, W. Zhan, M. R. Neupane, and R. K. Kawakami, *Nano Lett.* **17**, 3877 (2017).
- [53] G. B. Ventura, D. J. Passos, J. M. V. P. Lopes, and J. M. B. L. dos Santos, *J. Condens. Matter Phys.* **32**, 185701 (2020).
- [54] M. Buscema, J. O. Island, D. J. Groenendijk, S. I. Blanter, G. A. Steele, H. S. van der Zant, and A. Castellanos-Gomez, *Chem. Soc. Rev.* **44**, 3691 (2015).
- [55] M. Eginligil, B. Cao, Z. Wang, X. Shen, C. Cong, J. Shang, C. Soci, and T. Yu, *Nat. Commun.* **6**, 7636 (2015).
- [56] L. Xie and X. Cui, *Proc. Natl. Acad. Sci. USA* **113**, 3746 (2016).
- [57] S. Barraza-Lopez, B. M. Fregoso, J. W. Villanova, S. S. P. Parkin, and K. Chang, *Rev. Mod. Phys.* **93**, 011001 (2021).
- [58] X. Mu, Y. Pan, and J. Zhou, *npj Comput. Mater.* **7**, 61 (2021).
- [59] S. R. Panday, S. Barraza-Lopez, T. Rangel, and B. M. Fregoso, *Phys. Rev. B* **100**, 195305 (2019).
- [60] J.-M. Lihm and C.-H. Park, *Phys. Rev. B* **105**, 045201 (2022).
- [61] B. M. Fregoso, R. A. Muniz, and J. E. Sipe, *Phys. Rev. Lett.* **121**, 176604 (2018).